ACS OMEGA

http://pubs.acs.org/journal/acsodf

Article

Airflow, Fiber Dynamic Whipping, and Final Fiber Diameter in Flush Sharp-Die Melt Blowing with Different Air-Slot Widths

Jingjing Jia, Sheng Xie, and Caidan Zhang*

Cite This: *ACS Omega* 2021, 6, 30012–30018

Read Online

ACCESS | Metrics & More | Article Recommendations

ABSTRACT: Melt streams were attenuated into microfibers by high-speed airflow during melt blowing. The present work explored the effect of air-slot width on the fiber diameter and diameter evenness in flush sharp-die melt blowing. The airflow in different die melt blowing was first numerically simulated by the CFD approach. Then, the fiber dynamic whipping was captured by high-speed photography. Finally, a spinning experiment was implemented and the fiber diameters were measured. The result reveals that the sharp die with a larger air-slot width produces fibers with a larger diameter, but the uniformity is obviously better. This study reveals that the air flow, fiber whipping, and final fiber diameter are closely related to each other. The quality control of melt-blown fiber can be carried out by controlling the fiber whipping motion.

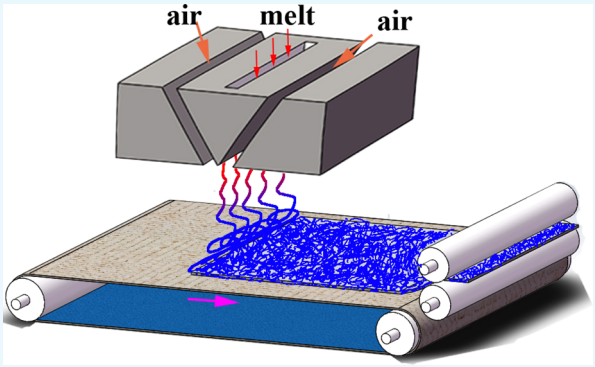

1. INTRODUCTION

As shown in Figure 1, polymeric melt streams are attenuated by high-speed airflow into nonwoven microfibers in the melt blowing process. Due to the fact that the melt-blown fibers have a diameter in the range of several micrometers[1] (fibers of 0.1 μm in diameter also can be made under some conditions[2]), melt-blown nonwoven fibers have crucial application in the filtration area and are the core component of face masks. The melt-blown technique receives unprecedented attention during the COVID-19 pandemic.

A lot of work has been done on exploring the melt-blown technique. Shambaugh and Tate[3,4] measured the air velocity and temperature during the melt-blown process by using a pitot tube and thermocouple, respectively, and provided empirical formulas for velocity and temperature decay. Sun et al.[5] and Wang et al.[6] measured the airflow by using a hot-wire anemometer; the measured results verified their numerical simulation results. A hot-wire anemometer was also applied for measuring the fluctuating velocity and temperature of melt-blown airflow.[7,8] The results showed that the temperature fluctuation revealed a regular profile like a sine or cosine curve; however, the velocity fluctuation was irregular. More recently, Xie et al.[9] explored the melt-blown air turbulence by particle image velocimetry (PIV); they found that the two ejected air jets from a pair of slots integrated immediately and began to form an S-shaped turbulent structure, and their work revealed the same structure of air turbulence and the specific fiber whipping motion[10] in slot-die melt blowing.

Due to the advantages of high efficiency and cost savings, computational fluid dynamics (CFD) technology was widely applied for exploring the melt-blown airflow. Krutka et al.[11] numerically simulated the melt-blown airflow, and the air recirculation in slot-die melt blowing was first demonstrated and discussed. Xie et al.[12] verified the air recirculation by a PIV experiment and found that the nose piece width was harmful to the fiber spinning during slot-die melt blowing. Chen et al.[13] numerically studied the effects of slot-die design parameters on air velocity and temperature distributions in the melt-blown flow field. The CFD method has been more and more applied into designing or optimizing a melt-blown die structure.[6,14−20] Sun and Wang[14] used the single-objective genetic algorithm and the CFD technology to achieve an optimized slot die. Wang et al.[6,15−17] designed an improved melt-blown die with stabilizing pieces by CFD simulation. Wang et al.[18] numerically investigated that adding an auxiliary nozzle was helpful to further decrease the fiber diameter. Hassan et al.[19] found that applying air constrictors around the primary air jets could keep the maximum air velocity and temperature in a longer distance. Tan et al.[20] and Blim et al.[21] studied the characteristic of the Laval-die melt-blown air flow by CFD simulation. In addition, melt-blown dies with louvers were designed,[22] and the spinning experiment verified the better effect of fiber attenuation.[23]

Received: August 27, 2021
Accepted: October 20, 2021
Published: October 27, 2021

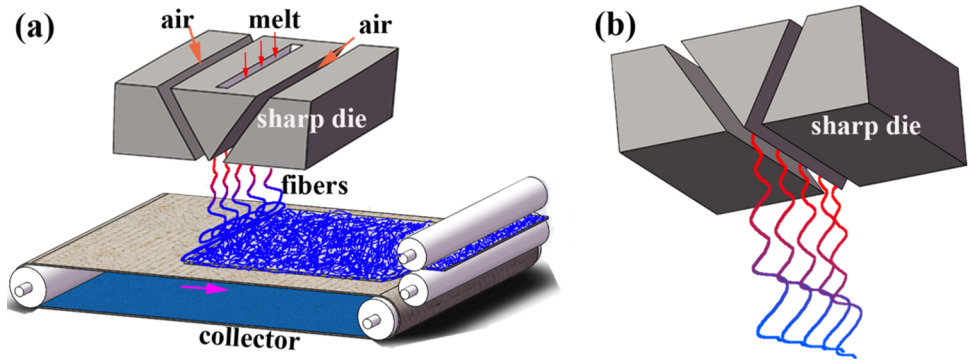

Figure 1. (a) Schematic of the melt-blown process. (b) Upward view of the flush sharp die and melt fibers extruded from the spinneret orifices. Here, five fibers are used for representing numerous fibers in industrial melt-blown equipment.

The fiber attenuation process also has attracted the attention of many researchers. Uyttendaele and Shambaugh[24] built an Euler-type model for the fiber attenuation process. Chen and Huang[25] considered the influence of temperature on melt density, heat capacity, and other factors and established a one-dimensional tensile model. Sun et al.[26] built a Lagrangian model for tracing the fiber attenuation during slot-die melt blowing. Sinha-Ray et al.[27] built a linearized theory of bending perturbation propagation over threadlines and polymer jets in melt blowing. Their work explained the onset of fiber whipping and explored severe bending instability leading to strong stretching and thinning during melt blowing. Chung and Kumar[28] suggested that melt inertia rather than melt rheology was the more dominant factor in controlling fiber shapes. Zhou et al.[29] revealed that disturbances were likely to become especially amplified at particular frequencies, with elasticity reducing the magnitude of the amplification but broadening the spectrum of frequencies susceptible to large amplification. The model of Tan et al.[30] predicted a strong dependence of fiber diameter on the air shear stress and variations in fiber diameter with viscoelasticity that are in qualitative agreement with the experimental results. Hübsch et al.[31] numerically verified the turbulent velocity fluctuations causing a random aerodynamic drag on the fiber jets, which was the crucial effect to close the gap between the computed diameter and the measured diameter. Shambaugh et al.[32] built a model to predict the effects of modified air fields on fiber formation. Their simulation showed that quenching can enhance online crystallinity, although fiber attenuation is reduced when quenching is used. Moreover, high-speed photography was also an effective method to explore the melt-blown process. Xie and Zeng,[10] Formoso et al.,[33,34] and Hao et al.[35] have done some work on exploring fiber whipping; the visualized fiber motion was beneficial to understanding fiber attenuation, fiber breakup, and shot formation during the melt-blown process.

The ultimate purpose of melt-blown research is to obtain melt-blown products with high quality. Fiber quality control is related to many factors, such as the diameter of melt orifice, polymer flow rate, airflow rate, and temperature. Hassan et al.[36] produced fibers with a diameter of less than 500 nm by using a small polymeric orifice diameter and low polymer throughput. Ellison et al.[1] were able to achieve some nanofibers with a mean diameter of 300−450 nm by using a single hole die with Γ (ratio of the air mass flux and the polymer mass flux) higher than 13. These methods will decrease the production efficiency and increase the energy consumption. In addition, the fiber quality was also decided by the melt-blown die structure. The spinning die is the core component of a melt-blown device due to the fact that the die structure has a crucial effect on the air flow field. Die types include slot die,[3,4,37] sharp die,[3,38−40] and annular die;[16,41] these dies were commonly used in the open literature. This paper focuses on the effect of flush sharp-die air-slot width on the fiber quality under the same inlet condition. The methodology adopted was to study the relationship among the characteristics of airflow field, fiber whipping, and final fiber diameter. Correspondingly, numerical simulation, high-speed photography, and electron scanning microscopy were used to implement this work.

2. DIE CONFIGURATION

Figure 1a shows the industrial melt-blown process; the extruded polymeric-melt streams are attenuated by high-speed air into microfibers. The upward view of the die shown in Figure 1b provides the detailed structure relationship between the die and fibers. The microfibers fly toward the collector and form melt-blown nonwoven fibers. In the present work, a single polymeric orifice melt-blown device was used. This device was equipped with a type of flush sharp die, and the fundamental die structure is shown in Figure 2a,b. Three flush-sharp dies were used in this work; these three sharp dies have the same structures of polymer orifice, d_0, and air-slot angle, θ, but have different air-slot widths, w. The detailed parameters of these three dies are shown in Table 1. All the dies have the same air-slot length of 7 mm along the nose piece or y-direction. Figure 2c shows the real die-0.5 mm, die-1.0 mm, and die-1.5 mm used in this work.

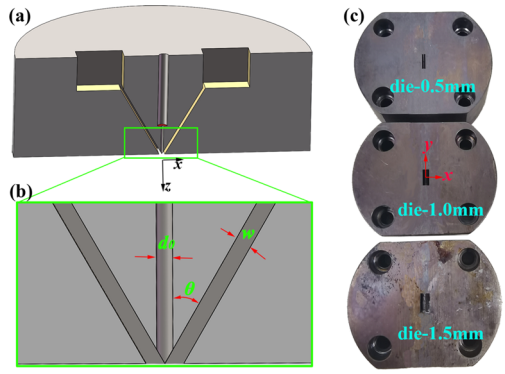

Figure 2. Fundamental structure of the flush sharp dies used in this work. (a) Cross section of the sharp die, (b) partial enlarged view of panel (a), and (c) real die-0.5 mm, die-1.0 mm, and die-1.5 mm.

https://doi.org/10.1021/acsomega.1c04689
ACS Omega 2021, 6, 30012−30018

Table 1. Name of Dies and Corresponding Structure Parameters

name of sharp die	d_0 (mm)	θ (°)	w (mm)
die-0.5 mm	0.5	30	0.5
die-1.0 mm	0.5	30	1.0
die-1.5 mm	0.5	30	1.5

3. NUMERICAL SIMULATION

3.1. Simulation Settings. As shown in Figure 3a, a two-dimensional model of airflow in the *x*-*z* plane was numerically

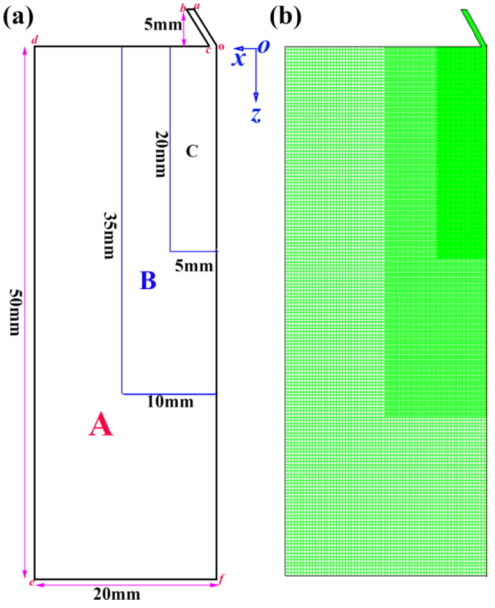

Figure 3. (a) Mesh region of the two-dimensional computational model. (b) Mesh grids in this two-dimensional region.

simulated, the inlet region (*o*-*a*-*b*-*c*) had a height of 5 mm, and the model below the inlet region had 50 mm height (length of *o*-*f*) and 20 mm width (length of *o*-*d*).

a-*b* was set as the velocity inlet boundary, *o*-*a* and *b*-*c*-*d* were the non-slip wall boundary, *d*-*e*-*f* was the outlet flow boundary, and *o*-*f* was the symmetric boundary. The velocity inlet was provided by compressible air, and the inlet velocities for die-0.5 mm, die-1.0 mm, and die-1.5 mm were 166.7, 83.3, and 55.6 m/s, respectively, which were calculated by dividing the gas volume flow rate (70 slm) by their respective air-slot cross section. The inlet air temperature was set to 220 °C.

In Fluent, the standard k-ε model[6,18] was used to calculate the two-dimensional flow field of the melt-blown slot dies. At the same time, the turbulence model parameters $C_{\varepsilon 1}$ and $C_{\varepsilon 2}$ were modified to 1.24 and 2.05, respectively.[6,11]

3.2. Grid Resolution Effects. As shown in Figure 3a, the whole computational region was labeled "A", and region "A" contains regions "B" and "C" (both B and C also contain the inlet region). The fundamental grid in "A" was established in Gambit when the model was built, and the grids in "B" and "C" were refined once and twice, respectively, in Fluent with the function of "adapt". Therefore, the grid size in "C" was half the size in "B" and was one-fourth that in "A". Figure 3b shows an example of grids in regions "A", "B", and "C".

The effects of changing the grid resolution were examined by running numerical experiments at different mesh sizes. The fundamental grid lengths of 0.4, 0.3, and 0.2 mm in region "A" were used (case 1, case 2, and case 3), and all three simulations were run using the same parameters and conditions. The velocity decay along the symmetry (*z*-axis) for these meshes is presented in Figure 4. Figure 4 shows that there is no

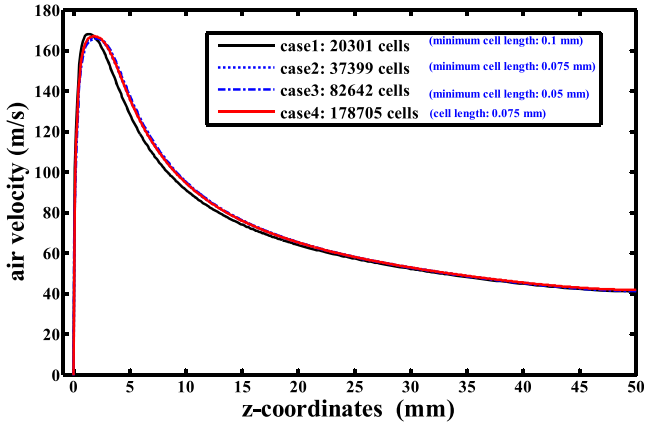

Figure 4. Numerically simulated air velocity along the *z*-axis for different grid resolutions.

distinguished change when the fundamental grid length is less than or equal to 0.3 mm; we also found that there was also no distinguished change between case 3 and the case where all grid lengths in the whole region were 0.075 mm (case 4). Therefore, in the formal numerical simulation, the fundamental grid was created with a length of 0.3 mm (case 2).

4. RESULTS AND DISCUSSION

4.1. Characteristics of Airflow in Different Sharp-Die Melt Blowing. Figure 5 shows the air velocities along the *z*-axis

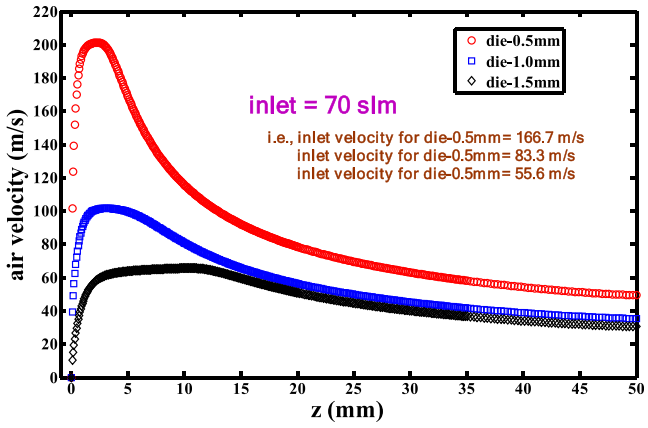

Figure 5. Air velocity along the *z*-axis for different die melt blowing with an inlet air volume flow rate of 70 slm. The inlet air volume flow rates for the three dies are equivalent to the inlet velocities of 166.7, 83.3, and 55.6 m/s for die-0.5 mm, die-1.0 mm, and die-1.5 mm, respectively.

for die-0.5 mm, die-1.0 mm, and die-1.5 mm melt blowing. All the simulations have the same inlet air volume flow rate of 70 slm. As shown in Figure 5, for all dies, the air velocities first increase to a peak and then decrease gradually with further distance from the die face, which is the fundamental characteristic for melt-blowing airflow.[3,4,10] It also can be found that the peak length increases with increasing sharp-die air-slot width. In addition, the maximum velocities are distinguished for different dies, and the maximum velocity decreases with increasing air-

https://doi.org/10.1021/acsomega.1c04689
ACS Omega 2021, 6, 30012−30018

slot width. For example, the maximum value is 200 m/s for die-0.5 mm but only 65 m/s for die-1.5 mm under the same inlet condition. Figure 5 indicates that the fiber attenuation effect decreases with a large air-slot width applied.

Figure 6 shows the air temperature along the z-axis for die-0.5 mm, die-1.0 mm, and die-1.5 mm melt blowing. The inlet air

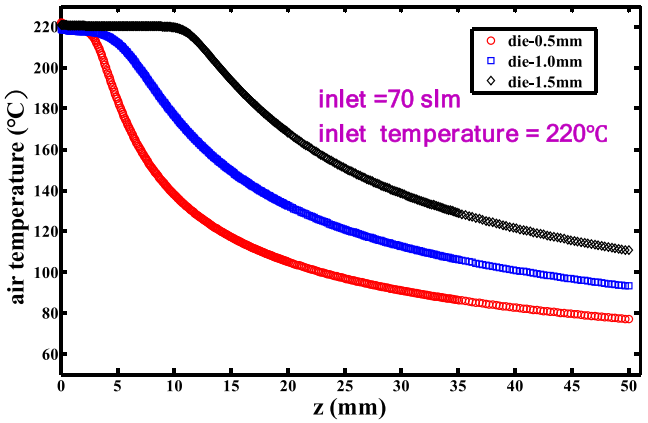

Figure 6. Air temperature along the z-axis for different die melt blowing with an inlet air volume flow rate of 70 slm.

temperature was 220 °C. The temperature curves are obviously different from the velocity curves in Figure 5. The temperature curves present a half unimodal distribution, i.e., the maximum temperature locates at z = 0 mm. Similar to Figure 5, the maintaining distance of the temperature peak increases with increasing sharp-die air-slot width, resulting in the finding that the air temperature is higher in the whole decay regions. For example, the temperature decreases to 75 °C at z = 50 mm for die-0.5 mm; however, the temperature is about 110 °C for die-1.5 mm. The characteristics of air temperature curves shown in Figure 6 indicate that the cooling rate of fiber melt slows down, which is beneficial to the fiber diameter adaptivity under the melt viscoelastic effect.

Figure 7 shows the air turbulence intensity along the z-axis for die-0.5 mm, die-1.0 mm, and die-1.5 mm melt blowing. The turbulence intensity curves present bimodal distribution, and the value of the second peak is higher than the first peak value. Moreover, it is distinguished that the turbulence intensity decreases with a larger air-slot width applied. Figure 7 reveals

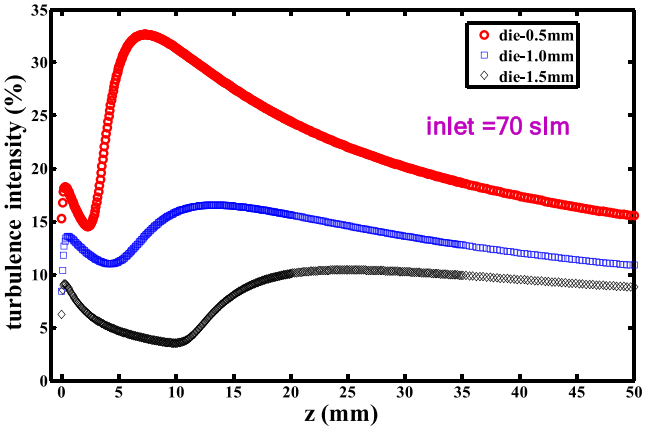

Figure 7. Air turbulence intensity along the z-axis for different die melt blowing.

that the fiber whipping motion in die-0.5 mm is more drastic than that in die-1.5 mm melt blowing. Note that random turbulence will have a negative effect on the uniformity of fiber attenuation.

4.2. Fiber Dynamic Whipping in Different Sharp-Die Melt Blowing. Figure 8 shows the fiber dynamic whipping in

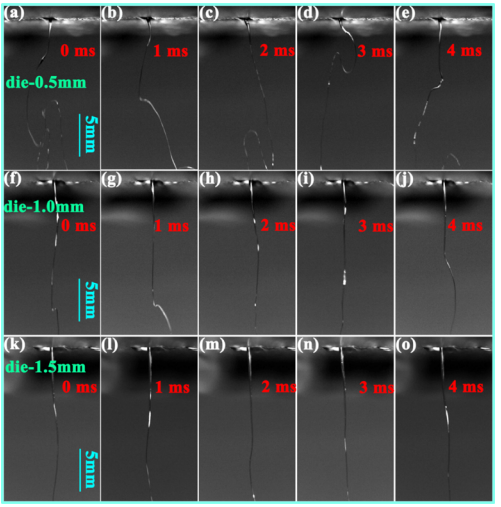

Figure 8. Fiber dynamic paths during three sharp-die melt blowing. (a–e) Fiber paths in die-0.5 mm melt blowing at time instants of 0, 1, 2, 3, and 4 ms. (f–j) Fiber paths in die-1.0 mm melt blowing at time instants of 0, 1, 2, 3, and 4 ms. (k–o) Fiber paths in die-1.5 mm melt blowing at time instants of 0, 1, 2, 3, and 4 ms. All the fiber paths were captured by a high-speed camera with a velocity of 5000 frames/s; the inlet air volume flow rate is 70 slm.

die-0.5 mm, die-1.0 mm, and die-1.5 mm melt blowing at successive time instants. Fiber whipping in die-0.5 mm melt blowing appears to be a fiber path with two groups of loops moving downward, which is similar with fiber whipping in slot-die melt blowing.[10] Figure 8f–j shows that in die-1.0 mm melt blowing, the fiber whipping loop still can be found at some time instants, but the loop is very small. Figure 8k–o shows that the structure of whipping loops disappears in die-1.5 mm melt blowing with the same inlet air volume flow rate. It also can be found that the smaller the air-slot width, the more intense and random the fiber whipping, which is attributed to the finding that the air turbulence intensity in sharp-die melt blowing with a small air-slot width is obviously higher than that in sharp-die melt blowing with a large air-slot width (as shown in Figure 7).

To characterize the fiber whipping intensity, the fiber whipping frequency and fiber envelope angle (or lateral whipping amplitude) were applied. The fiber whipping frequency was carried out by recording the fiber whipping locations at a certain z-level at successive time instants. Here, dimensionless fiber whipping relative positions at successive time series were recorded: if the fiber located at the right side of the center line (or z-axis), then the position was labeled as "1"; if the fiber located at the left side of the z-axis, then the position was labeled as "−1". The whipping frequency was obtained by counting the number of 1 or −1 in a period of 1 s. Figure 9 shows the fiber whipping dimensionless positions for die-0.5 mm, die-1.0 mm, and die-1.5 mm melt blowing. The fiber whipping frequencies in die-0.5 mm, die-1.0 mm, and die-1.5 mm melt blowing are 942, 692, and 458 Hz, respectively. The whipping frequency is positively correlated with air turbulence intensity.

https://doi.org/10.1021/acsomega.1c04689
ACS Omega 2021, 6, 30012−30018

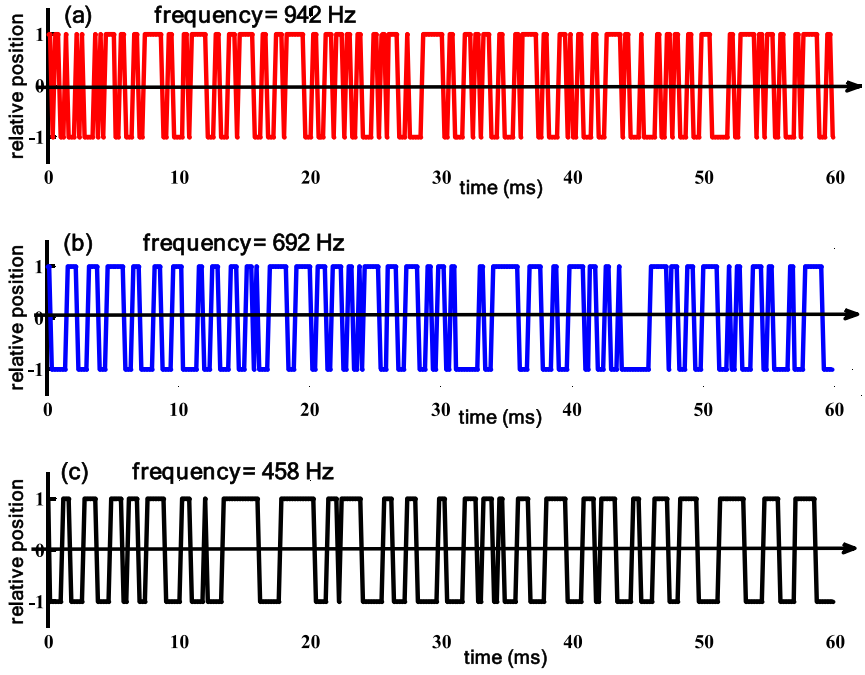

Figure 9. Dimensionless fiber whipping relative positions at successive time series for (a) die-0.5 mm, (b) die-1.0 mm, and (c) die-1.5 mm melt blowing. If the fiber whipping position located at the right of the center line, then the dimensionless position was labeled as "1"; otherwise, "−1" was labeled.

Figure 10 shows the fiber envelope angle in the three die melt blowing. The fiber envelope angle is the tip angle of the fiber

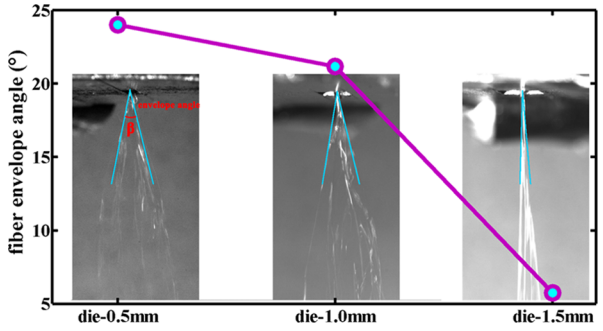

Figure 10. Fiber envelope angle during die-0.5 mm, die-1.0 mm, and die-1.5 mm melt blowing. The inset figures are the real fiber envelopes, which are captured by a high-speed camera with a low velocity of 50 frames/s.

envelope with the assumption that the fiber envelope is a triangle. Figure 10 reveals that the envelope angle decreases with a larger air-slot width used. Combined with Figure 9, the whipping frequency is probably positively correlated with the fiber whipping envelope angle.

4.3. Fiber Diameter for Different Sharp-Die Melt Blowing. Figure 11 shows the SEM images of fibers for die-0.5 mm, die-1.0 mm, and die-1.5 mm melt blowing at different inlet air volume flow rates. The fiber average diameter and corresponding standard deviation are shown in Figure 12a; Figure 12a shows that with increasing inlet air volume flow rate, the fiber diameter decreases for the three die melt blowing. Die-0.5 mm melt blowing produced the obviously smallest fiber diameter than die-1.0 mm melt blowing; however, the fiber diameter for die-1.0 mm melt blowing is a little bit smaller than the diameter for die-1.5 mm melt blowing. Figure 11 is

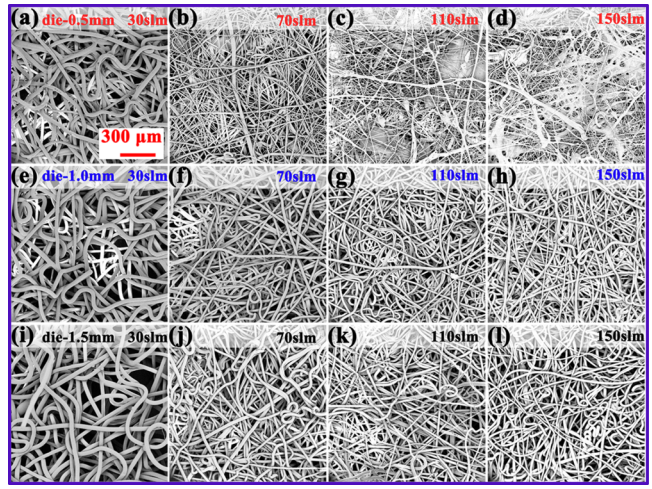

Figure 11. SEM images of the melt-blown fibers for the three dies with different inlet air volume flow rates. (a−d) SEM images for die-0.5 mm melt blowing with inlet air volume flow rates of 30, 70, 110, and 150 slm. (e−h) SEM images for die-1.0 mm melt blowing with inlet air volume flow rates of 30, 70, 110, and 150 slm. (i−l) SEM images for die-1.5 mm melt blowing with inlet air volume flow rates of 30, 70, 110, and 150 slm. The scale bars of all SEM images are the same as the scale bar in panel (a).

attributed to the finding that the air velocity in die-0.5 mm melt blowing is larger than the velocity in other two die melt blowing.

To represent the evenness of the fiber diameter, a parameter of coefficient of variance (CV) was applied and used; the CV is defined as the standard deviation divided by the average diameter. Figure 12b shows the CV of fiber diameter for the three die melt blowing; it reveals that the CV for die-1.0 mm and die-1.5 mm melt blowing is obviously smaller than that for die-0.5 mm melt blowing, and the CV for die-1.5 mm is slightly smaller than that for die-1.0 mm melt blowing. Figure 13 shows

https://doi.org/10.1021/acsomega.1c04689
ACS Omega 2021, 6, 30012−30018

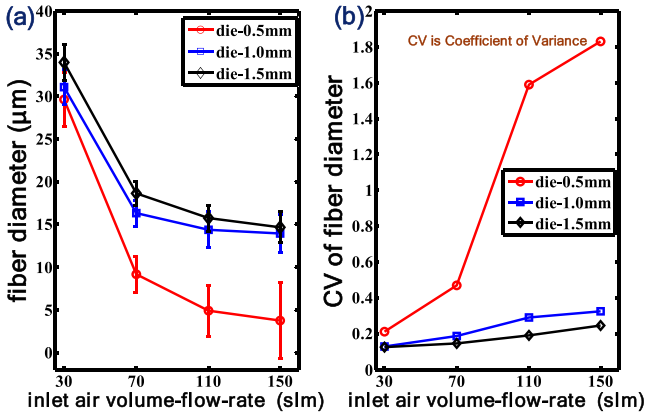

Figure 12. (a) Fiber diameter for three sharp-die melt blowing. (b) CV value of the fiber diameter for three sharp-die melt blowing. CV is the standard deviation divided by the mean diameter.

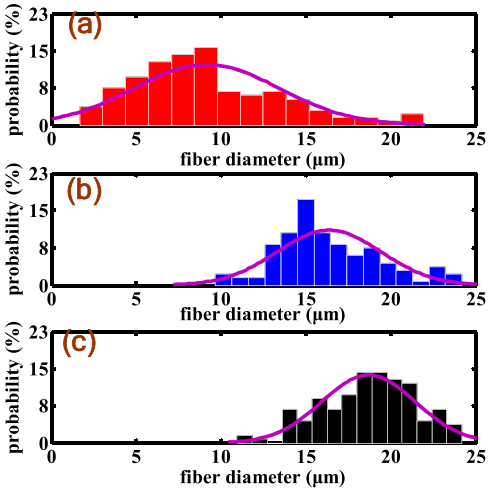

Figure 13. Probability distribution of the fiber diameters for (a) die-0.5 mm, (b) die-1.0 mm, and (c) die-1.5 mm melt blowing with an inlet air volume flow rate of 70 slm.

the fiber diameter probability distribution for the three die melt blowing under the condition of an inlet air volume flow rate of 70 slm. The distribution of fiber diameter becomes more and more concentrated from die-0.5 mm to die-1.5 mm, which is consistent with the conclusion of Figure 12b. The evenness of fiber diameter is decided by the air turbulence intensity; the higher air temperature in the sharp die with a larger air-slot width provides a probability that the bad evenness of fiber diameter can gradually become uniform under the effect of self-viscoelasticity. In addition, it seems that the fiber whipping frequency still has a close relationship with the fiber diameter evenness.

5. CONCLUSIONS

(1) Under the condition of the same inlet volume flow rate in flush sharp-die melt blowing, a die with a larger air-slot width is attributed to a smaller air velocity, smaller air turbulence intensity, and high air temperature.

(2) The fiber whipping frequency decreases with a larger air-slot width used. Sharp dies with air-slot widths of 0.5, 1.0, and 1.5 mm have whipping frequencies of 942, 692, and 458 Hz, respectively. In addition, the envelope angle decreases with a larger air-slot width used.

(3) The larger the air-slot width, the larger the fiber diameter produced; however, the uniformity of the fiber diameter is obviously better.

(4) There is a close relationship among air flow, fiber whipping, and fiber diameter in sharp-die melt blowing.

6. EXPERIMENTAL AND SIMULATIONAL SECTION

6.1. Experimental Conditions. Polypropylene with a 1500 melt flow rate provided by Hangzhou Chenda New Material Co., Ltd. (Hangzhou, China) was used as received. In this experiment, the polymer flow rate was fixed at 0.6 cc/min, the temperature of the polymer and the temperature of air were fixed at 220 °C, and the inlet air with volume flow rates of 30, 70, 110, and 150 slm was precisely controlled by a D07-91 gas flow meter (Beijing Sevenstar Flow Co., Ltd., Beijing, China); this gas flow meter had a maximum capability of 150 slm. The distance between the die and the collector was 20 cm.

6.2. Characterization. The fiber dynamic whipping was measured by an Acuteye-1M-2000CXP high-speed camera (Rocketech Technology Corp., Ltd., Changsha, China). This camera was equipped with a Tamron 90 mm prime lens and an HSLS-1000W-GY03 light source for improving the shooting sharpness. The fiber dynamic whipping was captured with a velocity of 5000 frames/s and an exposure time of 10 μs; the corresponding image size was 19.3 mm × 13.3 mm. Another capture velocity of 50 frames/s and exposure time of 1000 μs were used to efficiently measure the fiber envelope (amplitude of the fiber whipping path). The fiber whipping frequency and the whipping envelope angle were obtained by processing these high-speed images into Photoshop CS5 (Adobe, USA).

To characterize the fiber diameter, the morphology of the melt-blown nonwoven fibers was first scanned by a Phenom Pure scanning electron microscope (Phenom Scientific, Netherlands). For each sample, about 10 different places were scanned and captured into SEM images. Then, the fiber diameter was measured by importing the SEM images into Photoshop CS5. More than 150 discrete diameters were obtained for each sample.

6.3. CFD Software and the Computer. Due to the function of symmetry calculation, a half-model was created by Gambit 2.4.6. (ANSYS). Fluent 6.3.26 (ANSYS) and a computer with i7-7700 CPU (DELL) were used to calculate the airflow.

AUTHOR INFORMATION

Corresponding Author

Caidan Zhang − *Key Laboratory of Yarn Materials Forming and Composite Processing Technology of Zhejiang Province, Jiaxing University, Jiaxing 314001, China;* orcid.org/0000-0003-0307-3371; Email: caidanzhang@zjxu.edu.cn

Authors

Jingjing Jia − *School of Fashion and Design, Jiaxing Nanhu University, Jiaxing 314001, China;* orcid.org/0000-0002-3543-0292

Sheng Xie − *Key Laboratory of Yarn Materials Forming and Composite Processing Technology of Zhejiang Province, Jiaxing University, Jiaxing 314001, China;* orcid.org/0000-0002-0505-1988

Complete contact information is available at: https://pubs.acs.org/10.1021/acsomega.1c04689

https://doi.org/10.1021/acsomega.1c04689
ACS Omega 2021, 6, 30012−30018

Notes

The authors declare no competing financial interest.

■ ACKNOWLEDGMENTS

This work is supported by the National Natural Science Foundation of China (11702113), the Zhejiang Provincial Natural Science Foundation of China (LQ20E030014), the Open Project Program of Key Laboratory of Yarn Materials Forming and Composite Processing Technology of Zhejiang Province (MTC2020-15), and the Jiaxing Project of Science and Technology (2019AD32010).

■ REFERENCES

(1) Ellison, C. J.; Phatak, A.; Giles, D. W.; Macosko, C. W.; Bates, F. S. Melt blown nanofibers: Fiber diameter distributions and onset of fiber breakup. *Polymer* **2007**, *48*, 3306−3316.
(2) Shambaugh, R. L. A Macroscopic View of the Melt-Blowing Process for Producing Microfibers. *Ind. Eng. Chem. Res.* **1988**, *27*, 2363−2372.
(3) Tate, B. D.; Shambaugh, R. L. Modified Dual Rectangular Jets for Fiber Production. *Ind. Eng. Chem. Res.* **1998**, *37*, 3772−3779.
(4) Tate, B. D.; Shambaugh, R. L. Temperature Fields below Melt-Blowing Dies of Various Geometries. *Ind. Eng. Chem. Res.* **2004**, *43*, 5405−5410.
(5) Sun, Y. F.; Liu, B. W.; Wang, X. H.; Zeng, Y. C. Air-Flow Field of the Melt-Blowing Slot Die via Numerical Simulation and Multi-objective Genetic Algorithms. *J. Appl. Polym. Sci.* **2011**, *122*, 3520−3527.
(6) Wang, Y.; Zhou, J.; Gao, X. Numerical Analysis of Airflow Fields from New Melt-Blowing Dies for Dual-Slot Jets. *ACS Omega* **2020**, *5*, 13409−13415.
(7) Xie, S.; Han, W.; Jiang, G.; Chen, C. Turbulent air flow field in slot-die melt blowing for manufacturing microfibrous nonwoven materials. *J. Mater. Sci.* **2018**, *53*, 6991−7003.
(8) Xie, S.; Zeng, Y. Turbulent Air Flow Field and Fiber Whipping Motion in the Melt Blowing Process: Experimental Study. *Ind. Eng. Chem. Res.* **2012**, *51*, 5346−5352.
(9) Xie, S.; Jiang, G.; Ye, B.; Shentu, B. Particle Image Velocimetry (PIV) Investigation of Turbulent Airflow in Slot-Die Melt Blowing. *Polymer* **2020**, *12*, 279.
(10) Xie, S.; Zeng, Y. Online Measurement of Fiber Whipping in the Melt-Blowing Process. *Ind. Eng. Chem. Res.* **2013**, *52*, 2116−2122.
(11) Krutka, H. M.; Shambaugh, R. L.; Papavassiliou, D. V. Analysis of a Melt-Blowing Die: Comparison of CFD and Experiments. *Ind. Eng. Chem. Res.* **2002**, *41*, 5125−5138.
(12) Xie, S.; Jiang, G.; Wu, X.; Wang, Y.; Fang, H.; Shentu, B. Air Recirculation and Its Effect on Microfiber Spinning in Blunt-Die Melt Blowing. *Fibers Polym.* **2021**, *22*, 703−710.
(13) Chen, T.; Wang, X.; Huang, X. Modeling the Air-Jet Flow Field of a Dual Slot Die in the Melt Blowing Nonwoven Process. *Text. Res. J.* **2004**, *74*, 1018−1024.
(14) Sun, Y.; Wang, X. Optimization of Air Flow Field of the Melt Blowing Slot Die via Numerical Simulation and Genetic Algorithm. *J. Appl. Polym. Sci.* **2010**, *115*, 1540−1545.
(15) Wang, Y.; Ji, C.; Zhou, J. Experimental and numerical analysis of an improved melt-blowing slot-die. *E-Polymers* **2019**, *19*, 612−621.
(16) Wang, Y.; Wang, X. Investigation on a New Annular Melt-Blowing Die Using Numerical Simulation. *Ind. Eng. Chem. Res.* **2013**, *52*, 4597−4605.
(17) Cheng, Y.; Wu, L.; Chen, T. Numerical Simulation of the Air Flow Field in the Melt Blowing Process with an Auxiliary Nozzle. *Heat Transfer Res.* **2013**, *44*, 473−482.
(18) Wang, Y.; Qiu, Y.; Ji, C.; Wang, X.; Guan, F. The effect of the geometric structure of the modified slot die on the air field distribution in the meltblowing process. *Text. Res. J.* **2021**, No. 004051752110351.
(19) Hassan, M. A.; Anantharamaiah, N.; Khan, S. A.; Pourdeyhimi, B. Computational Fluid Dynamics Simulations and Experiments of Meltblown Fibrous Media: New Die Designs to Enhance Fiber Attenuation and Filtration Quality. *Ind. Eng. Chem. Res.* **2016**, *55*, 2049−2058.
(20) Tan, D. H.; Herman, P. K.; Janakiraman, A.; Bates, F. S.; Kumar, S.; Macosko, C. W. Influence of Laval nozzles on the air flow field in melt blowing apparatus. *Chem. Eng. Sci.* **2012**, *80*, 342−348.
(21) Blim, A.; Jarecki, L.; Blonski, S. Modeling of pneumatic melt drawing of polypropylene super-thin fibers in the Laval nozzle. *Bull. Pol. Acad. Sci.: Tech. Sci.* **2014**, *62*, 43−54.
(22) Shambaugh, R. L.; Krutty, J. D.; Singleton, S. M. Melt blowing dies with louvers. *Ind. Eng. Chem. Res.* **2015**, *54*, 12999−13004.
(23) Foley, K. A.; Shambaugh, R. L. Fiber spinning with airfields enhanced by airfoil louvers. *Text. Res. J.* **2019**, *85*, 3150−3158.
(24) Uyttendaele, M. A. J.; Shambaugh, R. L. Melt Blowing: General Equation Development and Experimental Verification. *AIChE J.* **1990**, *36*, 175−186.
(25) Chen, T.; Huang, X. Modeling the air drawing of polymer in the melt blowing nonwoven process. *Text. Res. J.* **2003**, *73*, 651−654.
(26) Sun, Y.; Zeng, Y.; Wang, X. Three-Dimensional Model of Whipping Motion in the Process of Microfibers. *Ind. Eng. Chem. Res.* **2011**, *50*, 1099−1109.
(27) Sinha-Ray, S.; Yarin, A. L.; Pourdeyhimi, B. Meltblowing: I-basic physical mechanisms and threadline model. *J. Appl. Phys.* **2010**, *108*, No. 034912.
(28) Chung, C.; Kumar, S. Onset of Whipping in the Melt Blowing Process. *J. Non-Newtonian Fluid Mech.* **2013**, *192*, 37−47.
(29) Zhou, C.; Tan, D. H.; Janakiraman, A. P.; Kumar, S. Modeling the melt blowing of viscoelastic materials. *Chem. Eng. Sci.* **2011**, *66*, 4172−4183.
(30) Tan, D. H.; Zhou, C.; Ellison, C.; Kumar, S.; Macosko, C. W.; Bates, F. S. Meltblown fibers: Influence of viscosity and elasticity on diameter distribution. *J. Non-Newtonian Fluid Mech.* **2010**, *135*, 892−900.
(31) Hübsch, F.; Marheineke, N.; Ritter, K.; Wegener, R. Random Field Sampling for a Simplified Model of Melt-Blowing Considering Turbulent Velocity Fluctuations. *J. Stat. Phys.* **2013**, *150*, 1115−1137.
(32) Shambaugh, B. R.; Papavassiliou, D. V.; Shambaugh, R. L. Modified Air Fields To Improve Melt Blowing. *Ind. Eng. Chem. Res.* **2012**, *51*, 3472−3482.
(33) Formoso, I.; Rivas, A.; Beltrame, G.; Larraona, G. S.; Ramos, J. C.; Antòn, R.; Salterain, A. Experimental study on the hot-melt adhesive pattern produced by melt blowing nozzle designs. *J. Ind. Text.* **2020**, 152808372097840.
(34) Formoso, I.; Rivas, A.; Beltrame, G.; Larraona, G. S.; Ramos, J. C.; Antòn, R.; Salterain, A. Experimental study of fibre breakup and shot formation in melt blowing nozzle designs. *J. Ind. Text.* **2020**, 152808372094927.
(35) Hao, X.; Huang, H.; Zeng, Y. Simulation of jet velocity in the melt-blowing process using the coupled air-polymer model. *Text. Res. J.* **2019**, *89*, 3221−3233.
(36) Hassan, M. A.; Yeom, B. Y.; Wilkie, A.; Pourdeyhimi, B.; Khan, S. A. Fabrication of nanofiber meltblown membranes and their filtration properties. *J. Membr. Sci.* **2013**, *427*, 336−344.
(37) Xie, S.; Han, W.; Xu, X.; Jiang, G.; Shentu, B. Lateral Diffusion of a Free Air Jet in Slot-Die Melt Blowing for Microfiber Whipping. *Polymer* **2019**, *11*, 788.
(38) Chelikani, S.; Sparrow, E. M. Numerical Simulations of Plane-Wall Coanda Effects for Control of Fiber Trajectories in the Melt-Blown Process. *Ind. Eng. Chem. Res.* **2013**, *52*, 11639−11645.
(39) Drabek, J.; Zatloukal, M. Influence of molecular weight, temperature, and extensional rheology on melt blowing process stability for linear isotactic polypropylene. *Phys. Fluids* **2020**, *32*, No. 083110.
(40) Krutka, H. M.; Shambaugh, R. L.; Papavassiliou, D. V. Effects of Die Geometry on the Flow Field of the Melt-Blowing Process. *Ind. Eng. Chem. Res.* **2003**, *42*, 5541−5553.
(41) Krutka, H. M.; Shambaugh, R. L.; Papavassiliou, D. V. Effects of the Polymer Fiber on the Flow Field from an Annular Melt-Blowing Die. *Ind. Eng. Chem. Res.* **2007**, *46*, 655−666.

https://doi.org/10.1021/acsomega.1c04689
ACS Omega 2021, 6, 30012−30018